Retinal Nerve Fiber Layer Assessment: Area versus Thickness Measurements from Elliptical Scans Centered on the Optic Nerve

Nimesh B. Patel, Xunda Luo, Joe L. Wheat, and Ronald S. Harwerth

Purpose. An evaluation of the retinal nerve fiber layer (RNFL) provides important information on the health of the optic nerve. Standard measurements of the RNFL consider only thickness, but an accurate assessment should also consider axial length, size of the optic nerve head (ONH), blood vessel contribution, and distance of the scan from the ONH margin. In addition, although most primate ONHs are elliptical, the circular scan centered on the ONH is the mainstay in both clinical and research analyses. The purpose of this study was to evaluate thickness and area measures of RNFL cross sections when axial length and ONH shape are included.

Methods. Circular, raster, and radial scans of left eye optic nerves were acquired from 40 normal rhesus monkeys (*Macaca mulatta*) using spectral domain optical coherence tomography. The disc margin was identified by manually selecting the RPE/Bruch's membrane opening and ONH border tissue. With a pixel-to-micrometer conversion computed from a three-surface schematic eye, RNFL scans were interpolated at 300 to 600 μm (50-μm increments) from the edge of the ONH. The thickness and area of the RNFL at each distance were obtained by custom programs. Blood vessels in the RNFL were selected and removed from the overall RNFL measures.

Results. The average RNFL thickness decreased systematically from 149 $\pm$ 12.0 μm for scans 300 μm from the disc margin to 113 $\pm$ 7.2 μm at an eccentricity of 600 μm ($P < 0.05$). In contrast, the cross-sectional areas of the RNFL did not vary with scan location from the disc margin (0.85 $\pm$ 0.07 mm^2 at 300 μm compared with 0.86 $\pm$ 0.06 mm^2 at 600 μm). Blood vessels accounted for 9.3% of total RNFL thickness or area, but varied with retinal location. On average, 17.6% of the superior and 14.2% of the inferior RNFL was vascular, whereas blood vessels accounted for only 2.3% of areas of the temporal and nasal RNFL regions.

Conclusions. In nonhuman primates, with appropriate transverse scaling and ONH shape analysis, the cross-sectional area of the RNFL is independent of scan distance, up to 600 μm from the rim margin, indicating that the axonal composition changes little over this range. The results suggest that, with incorporation of transverse scaling, the RNFL cross-sectional area, rather than RNFL thickness, provides an accurate assessment of the retinal ganglion cell axonal content within the eye. (*Invest Ophthalmol Vis Sci.* 2011;52:2477–2489) DOI:10.1167/iovs.10-6105

Glaucoma is a multifactorial group of optic neuropathies that ultimately lead to permanent vision loss if left untreated.[1] It has been estimated that by the year 2030, approximately 37 million individuals will be blinded by this disease.[2] The diagnosis of primary open-angle glaucoma is typically made from a clinical examination of the optic nerve and the nerve fiber layer and an evaluation of visual field sensitivity.[3–6] A major emphasis over the past few decades has been on early diagnosis and detection of disease progression, both of which require accurate and precise data to detect subtle optic neuropathy and assess changes over time.

Although functional assessment of vision is commonly used to evaluate optic neuropathies, intersubject and intrasubject variability can make detecting small defects or changes difficult.[7] Recent advances in imaging instruments allow for more objective measurements of various ocular diseases, and under optimum conditions, the measurements are far more precise. The most popular imaging modality, optical coherence tomography (OCT), uses low-coherence interferometry to acquire high-resolution images of the retina.[8] A recent advance in this technology, spectral domain OCT (SD-OCT) with eye tracking technology, provides faster, higher-resolution scans than the prior time domain methods (TD-OCT).[9–12] The resulting images are analyzed to provide thicknesses, and in the case of optic nerve diseases, the thickness of the retinal nerve fiber layer (RNFL) is commonly used to detect disease and monitor progressive changes.

The standard scan used to assess the RNFL is a circular one, 12° in diameter, centered on the optic nerve.[13–15] Analysis usually involves a RNFL thickness profile of the entire scan, along with sectoral and global (average) thicknesses that are compared to age-matched normative data. Several studies have shown these methods to be repeatable in both normal and glaucoma patients.[13,14,16] However, scan quality and placement have been shown to be important in thickness analysis, and control of these sources of error should be considered.[17–21]

In addition, to improve the accuracy of RNFL measures, factors such as axial length and the size and shape of the optic nerve head (ONH) should be considered.[22–28] Several studies (including the present study) demonstrate significant correlations between RNFL thickness measures and axial length.[22–24] For example, for 12° circular scans, the physical scan diameter increases with increasing axial length, because of ocular magnification factors (see Fig. 7).[29,30] As a result, the RNFL is usually thinner in eyes with longer axial lengths because the scans are farther from the ONH rim

From the College of Optometry, University of Houston, Houston, Texas.

Supported by National Eye Institute Grants R01 EY001139, K23 EY018329, and P30 EY007551 and by a John and Rebecca Moores Professorship.

Submitted for publication June 22, 2010; revised October 11, 2010; accepted November 10, 2010.

Disclosure: **N.B. Patel**, None; **X. Luo**, None; **J.L. Wheat**, None; **R.S. Harwerth**, None

Corresponding author: Nimesh Patel, University of Houston, College of Optometry, 4901 Calhoun Road, Houston, TX 77204; nbpatel2@uh.edu.

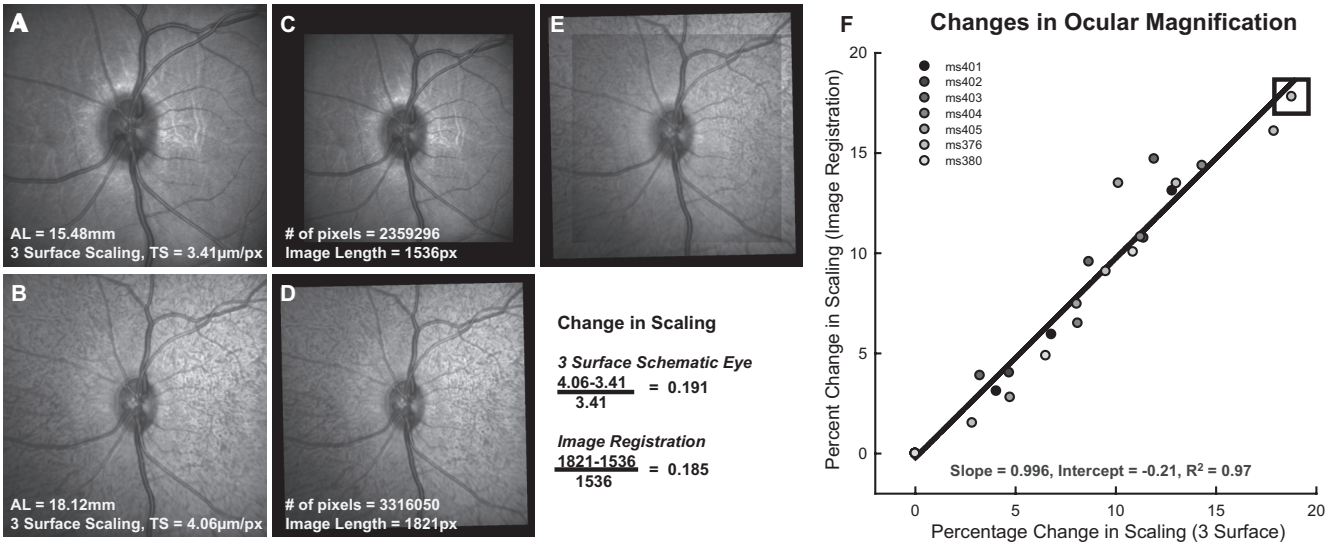

Figure 1. (**A**) Baseline 30° high-resolution SLO image centered on the optic nerve were used to register subsequent SLO images (**B**). The pixel content of the aligned scans (**C**, **D**), needed for accurate registration (**E**), was used to compute the change in ocular magnification. (**F**) The change in ocular magnification computed from image registration agrees with the change calculated using the three-surface schematic eye.

margin.[27,31] However, the variation in thickness with proximity to the rim margin should not represent a change in axonal content, but rather it should be a reflection of the convergence of axons to the ONH.

Rhesus monkeys are often used in vision research, as they can be trained for psychophysical tasks and have ocular and brain anatomy similar to that in humans.[32–38] Specifically, the nonhuman primate glaucoma model has provided invaluable insight into biochemical, functional, and structural changes that occur with glaucoma disease progression.[37–42] However, several differences between human and monkey eyes are important in the accurate assessment of structural content. Although the RNFL thickness profile and average thickness measures, using OCT technology, are similar to those in humans, the nonhuman primate has a significantly shorter axial length (19 mm) compared with that of humans (24 mm).[7,33,43] Hence, a standard 12° circular scan that has a circumference of 10.9 mm in humans would measure 8.01 mm in an adult *Macaca mulatta* eye. It is probable that the RNFL thickness profile is similar in the two species, as the optic nerves of rhesus monkeys are significantly smaller than those in humans, making the scan distance from the rim margin similar to that of humans.[7,39,44,45]

The inherent variation in density of RGC axons in the RNFL with proximity to the ONH causes uncertainty when RNFL thickness measurements are based on circular scans of a fixed angular diameter, unless transverse magnification effects are considered. In addition, the ONHs of both human and nonhuman primates are typically elliptical in shape, with the vertical meridian being larger than the horizontal[44,46] and, although nonhuman primates have significantly smaller ONH areas than humans, slightly larger quantities of axons normally pass into their neural canals.[39,44,45,47–52] Thus, there is a combination of ocular factors affecting the assessment of optic neuropathy from RNFL measures in nonhuman primates: smaller nerves with a larger quantity of axons, a shorter axial length, and the elliptical ONH shape.

For accurate assessment of the axonal content within the RNFL, the non-neuronal components (blood vessels and glial tissue) should be excluded from the total thickness. Al-

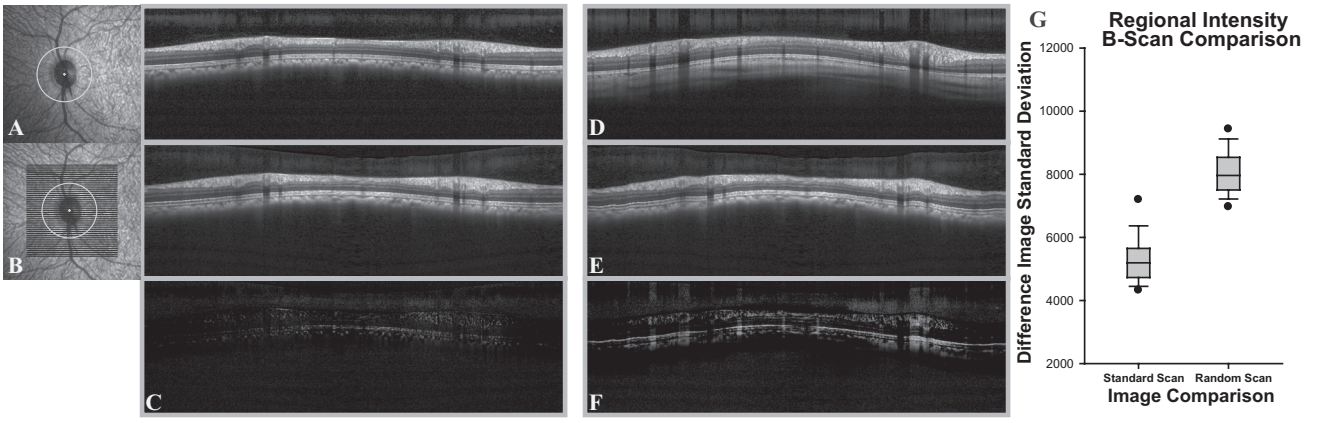

Figure 2. (**A**) SLO image with the standard scan pattern for RNFL analysis with high resolution B-scan from standard RNFL scan. (**B**) SLO image of raster scan with registered interpolated standard circular scan pattern. Individual A-scans of interpolated B-scans (**B**) were registered to the standard circular RNFL scan (**A**), and the difference image (**C**) was used for analysis. Similarly, A-scans of interpolated B-scans were registered (**E**) to a random standard RNFL scan from another animal (**D**) and subtracted (**F**). (**G**) The difference in image standard deviations between the two groups.

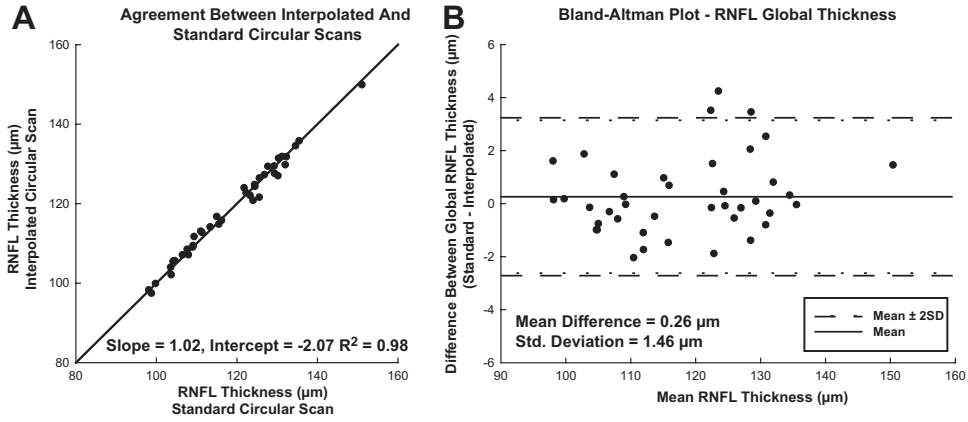

FIGURE 3. (**A**) Global RNFL thickness agreement between standard and interpolated 12° circular scans. (**B**) Bland-Altman plot comparing RNFL thickness of circular versus interpolated scans.

though glial tissue cannot be accounted for by current OCT imaging systems, blood vessels within the RNFL cast shadows in B-scans (Mardin CY, et al. *IOVS* 2009;50:ARVO E-Abstract 3333).[53] It is also interesting to note that most of the moderate- to large-caliber retinal blood vessels are in the superior and inferior sectors of the retina where the RNFL is thickest.[53]

Altogether, it is apparent that there are several optical and scanning factors that are likely to affect the accuracy of RNFL measurements for detecting and evaluating the stage of optic neuropathy by current OCT technology. These factors should be considered when using structural measures in nonhuman glaucoma models, where the shape of the eye is significantly different from that of the human. Therefore, the present investigation was undertaken to evaluate the effects of ocular biometry (refractive components and axial length), ONH characteristics (shape and area), and major retinal vessel area, on RNFL measurements by SD-OCT in rhesus monkeys of various ages. Some of the results of these studies have been presented in abstract form (Patel NB, et al. *IOVS* 2010;51:ARVO E-abstract 2104).

Material and Methods

Subjects

To include a large range of axial lengths, we used 40 rhesus monkeys ranging in age from 28 days to 23 years, the majority (32 monkeys) of which were less than 2 years of age. Seven of these animals were scanned multiple times over their first year of life, starting at 1 month of age. All animals had good systemic and ocular health, and only left eyes were included in the present study, which were the normal control eyes for other ongoing studies.[7,54–56] Experimental and animal care procedures were reviewed and approved by the Institutional Animal Care and Use Committee of the University of Houston. The use of animals for these experiments adhered to the ARVO Statement for the Use of Animals in Ophthalmic and Vision Research.

Optical Coherence Tomography

SD-OCT scans were acquired from animals under anesthesia. Animals <1 year of age were anesthetized with an intramuscular injection of ketamine (15–20 mg/kg) and acepromazine maleate (0.15–0.2 mg/kg), whereas animals >1 year of age were administered ketamine (20–25 mg/kg) and xylazine (0.8–0.9 mg/kg). The monkey's pupils were dilated to at least 4.5 mm with 1% tropicamide and 2.5% phenylephrine. Corneal hydration to preserve optical clarity was maintained by custom-designed, gas-permeable contact lenses. The animal's head was stabilized using mouth and occipital bars attached to a rotational mount, enabling appropriate eye alignment for scanning.

All scans were acquired by one of two of the authors using spectral domain optical coherence tomography (JLW, NBP; Spectralis HRA+OCT; Heidelberg Engineering, Heidelberg, Germany). For this study, three high-resolution scan patterns centered over the

TABLE 1. Comparison of RNFL Thickness Measures from Standard Circular RNFL Scans and Corresponding Interpolated RNFL Scan

	12° Circular Scan		Interpolated Scan		
Clock Hour	Mean Thickness (µm)	SD	Mean Thickness (µm)	SD	ICC
1	85.2	13.4	84.3	13.8	0.97
2	128.4	20.8	128.9	20.7	0.99
3	163.6	21.9	162.9	22.0	0.99
4	124.8	22.4	124.3	22.2	0.99
5	101.3	16.6	100.5	14.9	0.94
6	75.3	11.2	74.0	9.9	0.88
7	63.0	8.0	62.6	6.7	0.86
8	104.7	15.5	105.4	16.7	0.97
9	162.1	26.4	164.4	26.7	0.98
10	208.2	28.5	210.0	27.8	0.99
11	134.4	21.9	132.7	21.9	0.97
12	69.9	13.3	67.6	12.2	0.96
Global	118.4	12.5	118.1	12.1	0.99

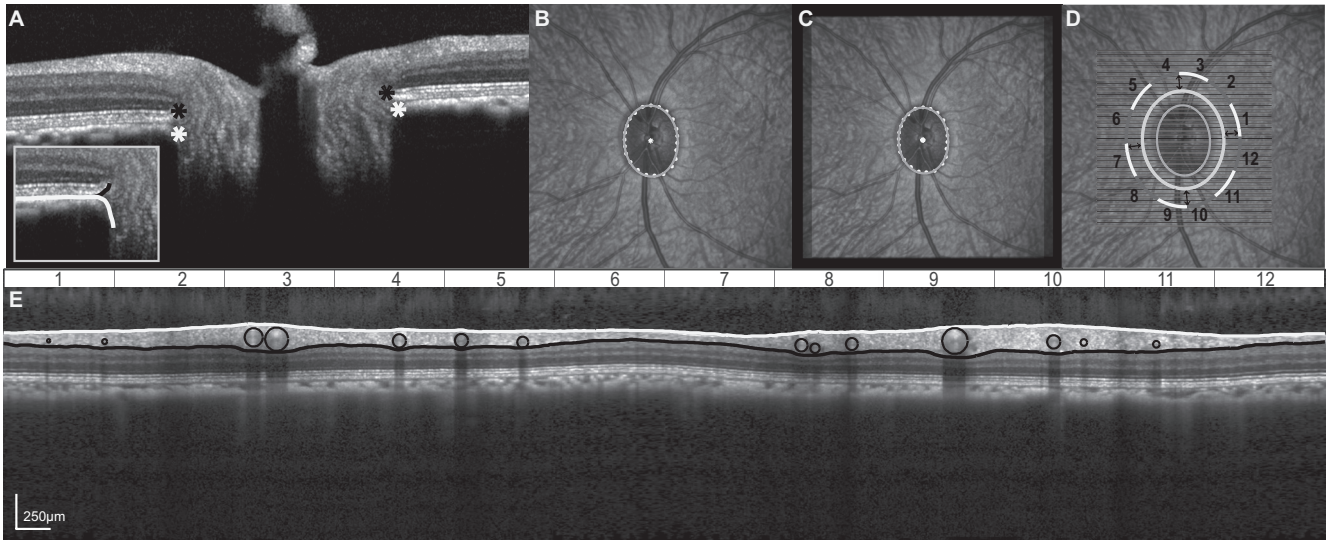

FIGURE 4. **(A)** The border tissue and RPEBruch's membrane were marked (*black* and *white asterisks*) on radial scans. **(B)** The corresponding NCO points on the IR-SLO image were plotted and fit with an ellipse. **(C)** The ONH best fit ellipse was registered to the raster scan SLO **(D)** Scans 300 to 600 μm from the ONH rim edge were interpolated from radial scans. **(E)** B-scans were analyzed using the same algorithm as that for standard scans.

optic nerve were acquired: the standard RNFL thickness scan using a 12° diameter circular pattern (1536 A-scans/B-scan), twelve 20° radial B-scans (1024 A-scans/B-scan), and a 20° × 20° horizontal raster grid composed of 49 B-scans (1024 A-scans/B-scan). For speckle noise reduction, B-scan averaging was set at 16 frames for all scan protocols. The scan data were exported in raw (.vol) files,

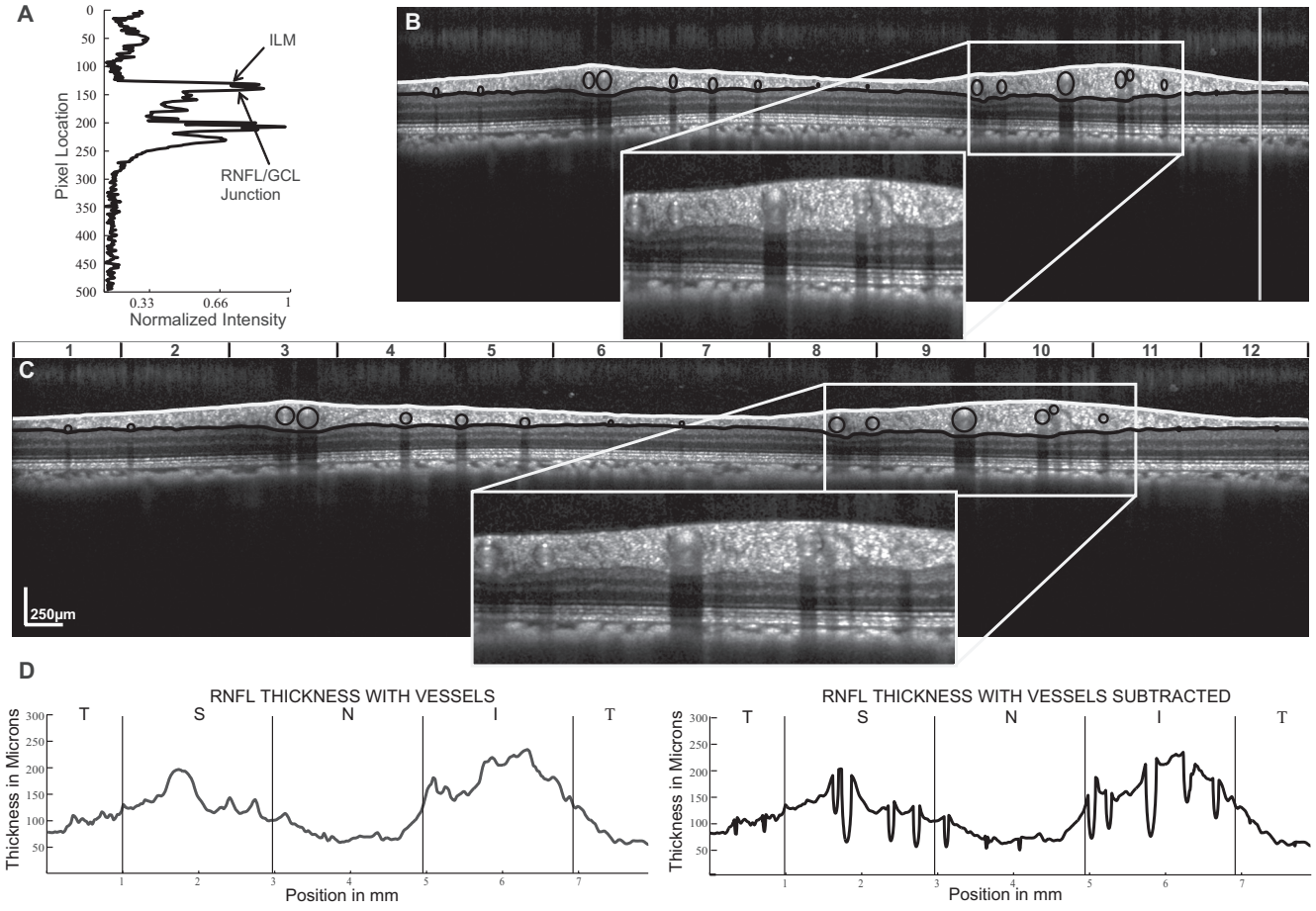

FIGURE 5. A-scan reflectivity profiles **(A)**, from RNFL scans **(B)** were used to determine the ILM and RNFL/GCL junction. The reflectivity profile illustrated is from the A-scan corresponding to the *white line* in the B-scan. Retinal vessels are illustrated for both the scaled and unscaled B-scans. Major retinal vessels within the RNFL of the scaled B-scan were identified by their shadows and fit within circles **(C)**. Standard TSNIT curves were created both with and without vessel subtraction **(D)**. RNFL measures were computed for the 12 sectors illustrated.

and converted to 16-bit/pixel B-scan images, using custom programs written in commercial software (MATLAB; The MathWorks, Inc., Natick, MA).

Ocular Biometry and Scaling

Biometric data including, corneal curvature, anterior chamber depth, and axial length for each monkey, were measured by a laser interferometer (IOLMaster; Carl Zeiss Meditec Inc., Dublin, CA). Crystalline lens parameters, including lens thickness, refractive index, and posterior and anterior lens radius, were interpolated from published normative data for monkey eyes.[33]

For each eye, data for transverse scaling were derived from a three-surface schematic eye, constructed using methods described by Bennett et al.[29,57] The model eye assumed a single-surface corneal (n = 1.336) homogenous refractive index for all optical structures and spherical refractive surfaces. The constructed eyes were used to calculate scan lengths and scaling factors at the posterior pole, based on the distance of the second nodal point to the retina, assuming a spherical retina[43]:

$$\text{Retinal scaling, } L = \frac{\pi}{180} \times N'F' \qquad (1)$$

where L is the length of retina in micrometers per angular degree from the nodal point, and $N'F'$ is the distance from the second nodal point to the retina.

In high-resolution Spectralis HRA+OCT scans (Heidelberg Engineering), the length of a 30° scan image is composed of 1536 pixels. Hence, a 20° B-scan is 1024 pixels in length, and a 12° circular scan has a diameter of 614 pixels. The transverse scaling for each pixel was calculated as:

$$\text{Transverse scaling } = \frac{L}{1536/30}. \qquad (2)$$

For example, the second nodal point (N') in an animal 5 years of age, with a corneal curvature of 5.8 mm, axial length of 18.01 mm, and anterior chamber depth of 3.35 mm, is 5.82 mm from the cornea, when a scan focus setting of +1.2 D is used. The calculated distance from the second nodal point to the retina is 12.19 mm, and the length of the retina scanned for each angular degree from the second nodal point is L = 212.8 μm/deg (equation 1). Scaling for this example is similar to and agrees with that of previously published four-surface schematic models of adult macaque eyes.[43] The transverse scaling (equation 2) for this example would be 4.16 μm/pixel, and a 20° B-scan would measure 4.26 mm (1024 pixels × 4.16 μm/pixel), and the circumference of the standard 12° scan would be 8.02 mm (π × 614 pixels × 4.16 μm/pixel). Axial scaling was determined from the instrument specifications (1 pixel = 3.87 μm). Each OCT B-scan was rescaled such that the length and width of each pixel was equal (see Figs. 4E, 5C).

In the seven animals observed longitudinally, we verified the use of the three-surface schematic eye for ocular magnification. Changes in the transverse scaling were compared with changes in the extent of the retina imaged with the scanning laser ophthalmoscope (SLO). SLO images from follow-up scans were registered using a generalized dual bootstrap iterative closest-point algorithm (i2k retina software; DualAlign LLC, Clifton, NY). The square root of the total-image pixel content in the registered images was used to determine the length of the registered image and the change in ocular magnification. Overall, there was a good relationship between the two scaling methodologies (Fig. 1, R^2 = 0.97, $P < 0.01$).

Interpolated Scan Validity: Circular Scans

It was necessary to develop and validate methods to create custom scans to investigate elliptical scan patterns. It is logical that custom B-scans scans could be created from a grid of raster scans using interpolation methods. For example, the Cirrus HD-OCT (Carl Zeiss

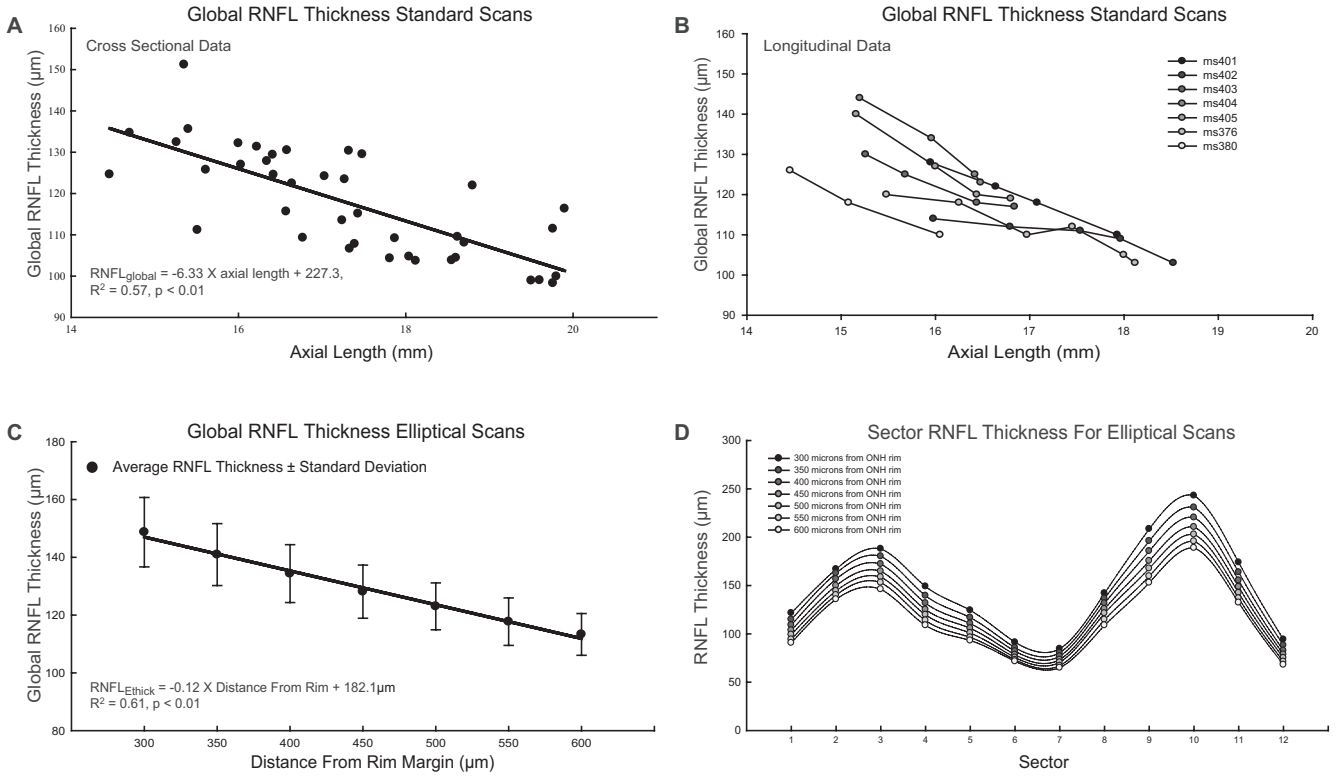

Figure 6. Global RNFL thickness from standard circular scans decreased systematically with increase in axial length, in both cross-sectional (**A**) and longitudinal (**B**) data. A systematic decrease in RNFL thickness also occurred with increasing distance from the rim margin in custom elliptical scans (**C**). This change in thickness was noted in all sectors of the ellipses evaluated (**D**).

Table 2. Linear Fit Parameters for Global 12° RNFL Thickness Change with Increase in Axial Length in Seven Animals Observed Longitudinally

Animal	Slope	Intercept
ms401	−13.5	343.4
ms402	−9.9	268.5
ms403	−8.4	257.8
ms404	−16.1	390.0
ms405	−9.1	273.3
ms376	−6.3	218.8
ms380	−3.8	176.2

Meditec, Dublin, CA) uses a cube of 200 × 200 A-scans to interpolate its standard RNFL circular scan. Using interpolation of circular scan paths from volume scans, the influence of scan decentration and comparability to TD-OCT methodology has been investigated.[20,21,58] Overall, these methods result in repeatable and reliable measurements of RNFL thickness.[59] However, scan interpolation from a cube with lower resolution in the vertical dimension (i.e., 49 lines in the 20° × 20° deg raster; 1024 pixels/raster line) should be validated. Therefore, to investigate the validity of interpolated B-scans, we compared standard circular scans and corresponding interpolated B-scans acquired on the same day (Fig. 2). The interpolation of a scan that is identical with the standard circular scan (Fig. 2A) requires transfer of the scan dimensions and coordinates of the circular scan onto the raster scan. The infrared SLO fundus images from the circular scan (Fig. 2A) and raster scan (Fig. 2B) were registered using a generalized dual bootstrap iterative closest-point algorithm (i2k retina; DualAlign LLC, Clifton, NY). Subsequently, the center and radius of the circular scan were extracted from the raw data file, and identical coordinates were determined on the registered raster fundus image. A-scans from identical locations to the standard circular scan were interpolated from the raster cube by linear interpolation (Fig. 2B). The similarity of the B-scan images and the RNFL thickness values were used for comparison.

For a more analytical comparison to determine whether the methods of extracting circumpapillary RNFL thicknesses from raster data caused substantive alterations of the images, the fidelity of interpolated circular scans was assessed by comparing differences in regional intensities in the retinal images. Individual A-scans from the interpolated B-scan were registered to the standard or random scans by shifting each A-scan to the location with the highest cross correlation.

The results of the image analyses, illustrated in Figure 2, demonstrate that when the extracted circle scan (I_{Rc}) (Fig. 2B) is subtracted from the standard scan (equation 3) of the same monkey (I_c) (Fig. 2A), the difference image (I_d) (Fig. 2C) contains little data. On the other hand, when the extracted scan (Fig. 2E) is subtracted from the standard scan of one of 10 randomly selected animals (Fig. 2D), the difference scan (Fig. 2F) contains many larger values. To quantify the comparisons of same or different subjects, the standard deviations of pixel values across the difference images (Fig. 2C, 2F) were used for statistical analysis. For 16-bit images, the units for each pixel range from 0 (black) to 65,535 (white):

$$I_d = \text{abs}[I_{Rc}(x, y) - I_c(x, y)]. \quad (3)$$

The standard deviations should be smaller for similar images, and it was found that the SDs of difference images (Id) were significantly less when interpolated B-scans were compared to standard scans from the same eye (5321.2 ± 851) than when compared to a random standard scan (8296.7 ± 1563; $P < 0.01$). These standard deviations represent a coefficient of variation (CoV) of 8.1% for comparison to a scan from the same eye and 12.7% for a scan from a random eye.

Although the intensity data demonstrate that the standard and interpolated scans are qualitatively comparable, it is also important to compare RNFL thicknesses to determine whether the segmentation routines retain the retinal morphology information. The data presented in Figure 3A, illustrate that global RNFL thickness measures from interpolated scans and standard scans correlated highly ($R^2 = 0.98$, $P < 0.01$). The Bland-Altman analysis (Fig. 3B) also demonstrates agreement of measures, with a mean difference of 0.26 μm and 95% limits of agreement of −2.6 to 3.1 μm. In addition, the intraclass correlation (ICC) for global thickness measures was 0.99 and >0.75 for all 12 clock hour sectors (Table 1). Based on these results, calibration equations were not required, as they are for systematic differences between time domain and spectral domain RNFL measures obtained with similar methodologies.[58] Overall, the statistical analysis confirms that the interpolated scans have excellent quantitative agreement with standard scans using SD-OCT technology and similar agreement should hold for elliptical scans extracted from raster data.

Scan Interpolation and Analysis: Elliptical Scans

For construction of elliptical scans, the shape and size of the optic nerve had to be determined. Locations along the ONH rim margin were marked manually by identifying the border tissue and RPE/Bruch's membrane, as visualized in the radial B-scans centered on the optic nerve (Fig. 4A, white and black asterisks). When necessary because of obstruction of features by the shadows of blood vessels, points were selected directly on the raster scan infrared SLO fundus image.[44,60] For the purposes of this study, both boundaries were fit with a best-fit ellipse, and the ellipse for the neural canal opening (NCO) was used for scan interpolation (equation 4 and Fig. 4B). The ONH outline was then transferred to the raster scan image (Fig. 4C) after the fundus images of the radial and raster scans had been aligned using the retinal registration software (i2k Retina; DualAlign, LLC). The major and minor axes of the fitted ellipse were used to calculate the area of the nerve and as a reference to create

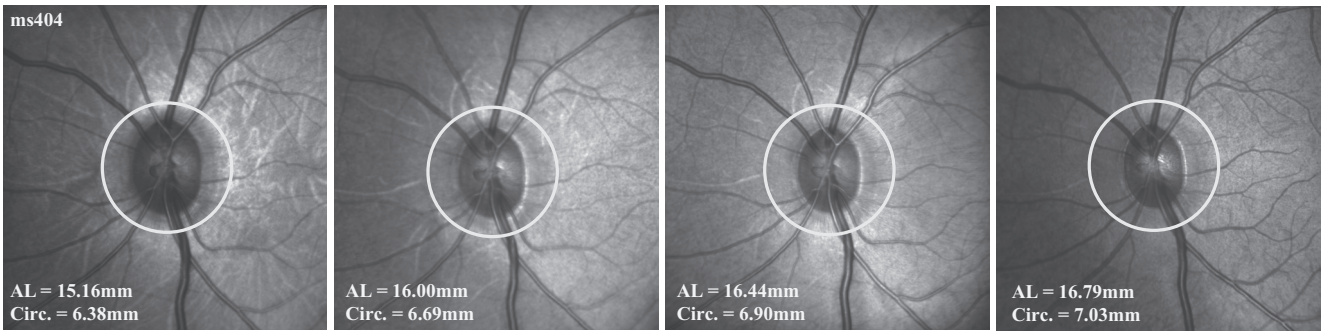

Figure 7. Standard RNFL scan path for an infant rhesus monkey at four separate scanning sessions. AL, axial length; circ., circumference.

TABLE 3. Best Linear Fit Data for Global RNFL Thickness from Elliptical Scans and Axial Length

Scan Distance From Rim	Slope	R^2	*P*
300	−1.95	0.04	0.2
350	−1.24	0.02	0.36
400	−1.35	0.03	0.29
450	−1.16	0.03	0.31
500	−0.94	0.02	0.36
550	−0.96	0.02	0.35
600	−0.65	0.01	0.47

larger ellipses (equation 4). Concentric ellipses with eccentricities of 300 to 600 μm from the ONH rim margin in 50 μm steps (Fig. 4D) were constructed by increasing the lengths of major and minor axes in equal increments:

$$\frac{(x-b)^2}{a^2}+\frac{(y-k)^2}{b^2}=1$$

$$\text{Ellipse}_{\text{area}} = \pi \times a \times b \quad (4)$$

$$\text{Ellipse}_{\text{center}} = (b, k)$$

where (b, k) represents the center of the ellipse, (a, b) represent the major and minor ellipse axis, and (x, y) are point coordinates on the ellipse. The circumference of each constructed ellipse was estimated using Ramanujan's approximation (equation 5)[61]:

$$\text{Circumference}_{\text{ellipse}} \approx \pi(a+b)\left[1+\frac{3\left(\frac{a-b}{a+b}\right)^2}{10+\sqrt{4-3\left(\frac{a-b}{a+b}\right)^2}}\right]. \quad (5)$$

Data for the B-scans corresponding to each of the elliptical scan paths were interpolated from the raster B-scan data, with a resolution of 1536 interpolated A-scans (i.e., the number of A-scans acquired with the standard high-resolution circular scan). The elliptical B-scans were scaled to 1 pixel:1 μm, based on the length of the B-scan corresponding to the computed circumference of the ellipse, as illustrated by the example (Fig. 4E) of an OCT scan derived for an ellipse 600 μm from the ONH rim.

RNFL Quantification

Borders to segment the RNFL for both standard and interpolated scans were determined using custom-written computer programs (MATLAB; The MathWorks). To improve RNFL segmentation, B-scans were denoised with a Haar two-dimensional stationary wavelet, and convolved with a Gaussian filter with an SD of 4. Signal intensity profiles for each A-scan from the original B-scan (Fig. 5A) and denoised B-scan were used iteratively to determine the inner limiting membrane (ILM) and RNFL/ganglion cell layer (GCL) junction. The ILM, shown by the white line (Fig. 5B) was determined as the first peak in each A-scan intensity profile (Fig. 5A), whereas the RNFL/GCL junction was defined as the subsequent region with a dampening of reflectivity, illustrated by the black line (Fig. 5B). Small errors in segmentation, especially noted in regions were the RNFL signal was poor and around the major retinal vasculature, were manually corrected.

The cross-sectional images in Figure 5 illustrate the effect of appropriate transverse scaling by comparison of the unscaled image (Fig. 5B)

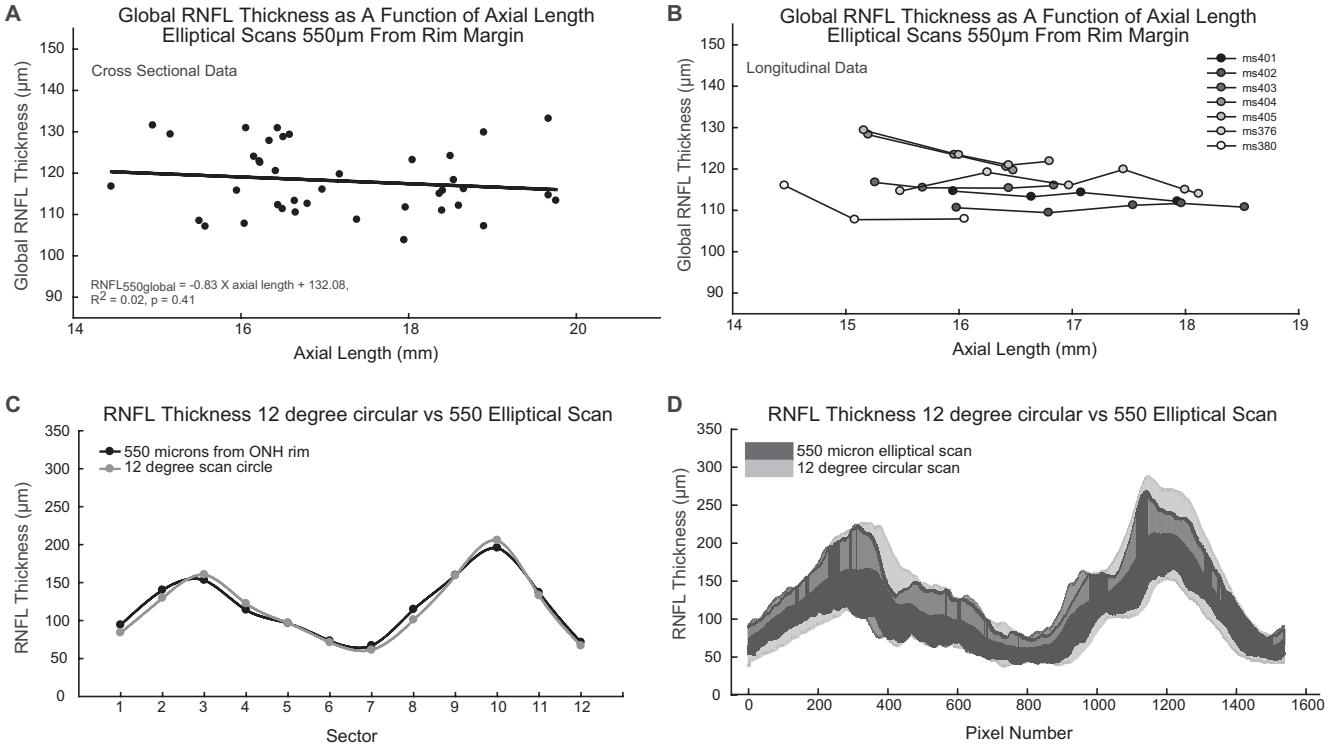

FIGURE 8. Elliptical scans did not correlate with axial length. The plots illustrate the relationship of global RNFL thickness with axial length for the 550-μm elliptical scan for both the cross-sectional (**A**) and longitudinal data (**B**). The 550-μm elliptical scan was most similar to the 12° circular scan (**C**). Scans of 550 μm had less variation in thickness than did standard 12° scans (**D**). Illustrated are the 95% confidence limits for TSNIT plots for both scan types.

TABLE 4. Thickness and Area Changes in Global RNFL Measures after Vessels Were Eliminated from the RNFL

Scan Path	RNFL Global Thickness (μm)	Change in Thickness with Vessel Removal	Percentage Change	RNFL Global Area (μm^2)	Change in Area with Vessel Removal	Percentage Change
300	148.9	13.5	9.1	850270.7	77083.3	9.1
350	141.2	12.9	9.1	851055.7	77943.4	9.2
400	134.5	12.4	9.2	852463.1	79143.2	9.3
450	128.3	11.8	9.2	853083.7	78861.5	9.3
500	123.1	11.4	9.3	857399.1	79905.5	9.3
550	117.9	11.2	9.5	857837.5	81573.3	9.5
600	113.5	10.6	9.3	860812.7	80515.7	9.4
12°	115.2	10.2	8.8	846114.3	72893.4	8.6

Data for elliptical scans 300 to 600 μm from the rim margin and the standard 12° circular scan.

and the scaled image (Fig. 5C). After B-scans are scaled to 1 pixel:1 μm, the vascular structures within the retinal nerve fiber layer, identified by the shadows cast on the underlying layers, are the expected circular shape, instead of the vertical ovals in the unscaled images (cf., insets in Figs. 5B, 5C).[53] For further image analysis, the borders of each shadow were manually marked along with the center of the visible vessels within the B-scan. A circular region with a center marked for that of the vessel and a diameter equivalent to the width of the shadow was used to determine the vessels' contribution to the RNFL thickness or area. To prevent negative values for RNFL measures, only portions of the circle within the borders of the ILM and RNFL/GCL junction were used. An example of the contributions of blood vessels to RNFL thickness is presented in Figure 5D by RNFL TSNIT data for the scaled images before (left panel) and after the subtraction of blood vessels (right panel). The effect of removing the blood vessels is apparent by inspection of the insets for Figures 5B and 5C, the inferior sector that illustrates the relative thinning of the TSNIT data (Fig. 5D) in the specific regions of blood vessels.

For analysis of thickness or area, global thickness was determined by the average RNFL thickness measured from all A-scans within the B-scan and sector thicknesses were based on the average RNFL thickness from A-scans within each of the 12-clock-hour regions. RNFL areas were calculated by multiplying the average RNFL thickness, in micrometers, by the length of the scan or of a sector of the scan, in micrometers.[25]

RESULTS

RNFL Thickness Measures

Axial lengths for the rhesus monkeys in this study ranged between 14.5 and 19.9 mm and were normally distributed with a mean of 17.28 ± 1.38 mm. These values were appropriate for the ages of the animals used for the study.[33] The influence of ocular magnification is clearly demonstrated by the relationship between global RNFL thickness and axial length. With the standard scan used without transverse scaling, the animals with longer eyes had significantly thinner RNFLs ($R^2 = 0.57$, $P < 0.01$; Fig. 6A), with a linear regression slope of -6.33 μm/mm. Similarly, global RNFL thickness in each of the seven longitudinally observed infant animals decreased systematically as their eyes lengthened (Fig. 6B) at rates that varied from -6.3 to -16.1 μm/mm, with a mean of -9.6 μm/mm (Table 2). An example of the change in the relationship between the standard scan location with respect to the ONH as the axial length increases during normal growth is presented in Figure 7, for one young monkey (ms404; see Fig. 6B). It is apparent that the distance of the OCT scan from the ONH rim increases with axial length. Therefore, the change in RNFL thickness with axial length is likely to be a methodological artifact rather than a reflection of the neuronal composition. Specifically, the axonal content of the RNFL should not vary over a short period of aging or with axial length, and thus it is likely that the measurements represent an effect of scan location.

The importance of the scan path distance to the rim of the ONH is exemplified by the thickness measures from the elliptical scans (Fig. 6C). The means of the population data at each scan distance illustrate a decreasing global RNFL thickness with increasing eccentricity (300–600 μm) from the ONH rim margin ($R^2 = 0.61$, $P < 0.01$; Fig. 6C). The systematic and consistent relationship is strongly supported by the ICC of 0.34 for global thickness versus scan distance. The significant differences in mean thickness as a function of scan location were confirmed by repeated-measures ANOVA ($F_{(2.19,\ 85.4)} = 1014.1$, $P < 0.01$). The results of the ICC and ANOVA analyses for each the 12-clock-hour sectors (Fig. 6D) were in agreement with the global thickness results.

Although RNFL thickness varied with scan eccentricity (Fig. 6C), when the elliptical scans were placed a constant distance from the ONH rim the relationship between RNFL thickness and axial length for any given eccentricity was not significant (Table 3, Figs. 8A, 8B). In fact, the global RNFL thickness measures with elliptical scans located 550 μm from the ONH rim were similar to the 12° circular scans (Fig. 8C), although the cross-sectional variability of the circular scans was larger (CoV = 11.0%) than that of the elliptical scans (CoV = 6.9%, Fig. 8D). In addition, the residuals for the best fit for elliptical scans 500 μm from the rim margin had a smaller variance (51.32) than for 12° scans (81.74). Thus, these data support the hypothesis that the relationship between RNFL thickness and axial length occurs because the proximity of standard OCT scan paths to the ONH rim vary with axial length.

Vascular Component

In the assessment of glaucomatous neuropathy, especially for the assessment of progression, it may be important to separate

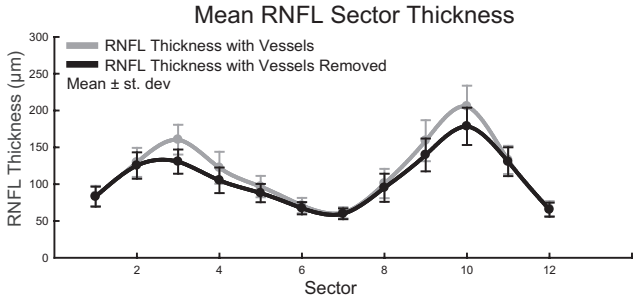

FIGURE 9. Vessel contribution to RNFL thickness was greatest in the superior and inferior portions. Shown are the average RNFL thicknesses, with and without vessel compensation, in each clock-hour sector.

TABLE 5. Vessel Contribution to Sector Thickness for Standard RNFL Scans

Sector	Vessel Contribution (μm)	Percentage RNFL
1	1.1 ± 1.8	1.25
2	4.3 ± 5.1	3.35
3	29.9 ± 11.7	18.63
4	17.0 ± 11.5	13.88
5	8.8 ± 5.6	9.13
6	3.8 ± 4.3	5.30
7	1.4 ± 2.1	2.28
8	5.7 ± 6.1	5.69
9	19.3 ± 13.5	12.17
10	27.1 ± 14.1	13.19
11	2.4 ± 4.0	1.80
12	1.4 ± 2.1	2.07
Global	10.2 ± 2.5	8.80

the neuronal and non-neuronal components of the RNFL. To determine the extent of one non-neuronal vascular component, we identified the major retinal vasculature visible within the high-resolution OCT images and removed it from the thickness and area measures. Across the 40 subjects, the major retinal vascular contribution to the mean RNFL thickness for standard scans was 10.2 ± 2.5 μm (Table 4). The amount of blood vessel contribution to RNFL thickness was larger for the superior and inferior portions, compared with the temporal and nasal RNFL, and these segments were the most affected by the removal of the vessels (Fig. 9, Table 5). For elliptical scans, removing the major retinal vasculature resulted in a greater reduction of global RNFL thickness for scans closer to the rim margin (repeated-measures ANOVA, $F_{(4.55,\ 182)} = 37.371$; $P < 0.01$). However, the proportional change in RNFL measures was not altered significantly with scan distance (repeated measures ANOVA, $F_{(6,\ 240)} = 0.998$; $P = 0.43$).

Area Measures

The next logical refinement of RNFL assessment was to translate the thicknesses to RNFL area values. RNFL area measures should provide a better quantification of axonal content, which should not change with the region scanned in a given eye and should provide an accurate assessment of axonal losses with age or glaucoma. The cross-sectional areas were calculated by multiplying the mean RNFL thickness by the ellipse circumference, for circular scans determined by the scan radius and for elliptical scans, by using Ramanujan's approximation (equation 5).[61]

For standard RNFL circular scans, the correlation between RNFL area and axial length was not significant ($R^2 = 0.07$, $P = 0.11$), although there was a slight trend toward larger global RNFL area measures with increasing axial length. In agreement with the results for circular scans, cross-sectional RNFL areas for the custom elliptical scans did not change significantly with increasing distance from the ONH rim margin (Fig. 10A; $R^2 = 0.002$, $P = 0.49$). The ICC for global RNFL area measures was 0.97 for the seven eccentricities from the ONH rim analyzed. Repeated-measures ANOVA with Greenhouse-Geisser estimates for sphericity also indicated no significant relationship between global RNFL area measures for the seven elliptical scan distances ($F_{(3.899,\ 152)} = 1.732$; $P = 0.15$). Area measures for all 12 sectors analyzed showed similar results (Fig. 10B). CoV measures of variance were similar for both thickness and area measures for elliptical scans. A significant reduction in variation was also achieved for the standard scan when using area measures (Table 6). These findings are in line with the premise that the variation in thickness with eccentricity from the OHN rim is a result of changing the length of the scan, and thus scans with smaller circumferences have larger thicknesses to encompass a constant number of axons entering the ONH. In addition, within the peripapillary region analyzed in this study, the ganglion cell density was relatively low, and a large change in axonal content was not expected.[62] However, when the scan eccentricity is significantly large, axons from cell bodies more proximal to the ONH are not included in the measure, and the RNFL area is smaller.

ONH Parameters

The transverse scaling should provide a more accurate measurement of the ONH size. The OHNs of all the animals imaged are better described as ellipses than circles, with the major axis oriented vertically. The average major and minor axis dimensions were 0.688 ± 0.057 and 0.522 ± 0.044 mm, respectively, with a mean ratio of vertical/horizontal axes of 1.32 ± 0.06. ONH areas were calculated from the fitted ellipse ($A = a \times b \times \pi$) that should be a close approximation to the opening of the neural canal. Although the ranges of ages and axial lengths of the 40 monkeys were quite broad, the intersubject variability of ONH area measures was small. The mean ONH area was 1.14 ± 0.18 mm^2 with a range of 0.78 to 1.48 mm^2. The ONH size was statistically related to RNFL global area ($R^2 = 0.19$, $P < 0.01$; Fig. 11), but not to axial length ($R^2 = 0.06$, $P = 0.14$). This result is not surprising, as we would expect larger optic nerves in eyes with a greater number of RGC axons.

DISCUSSION

The results demonstrate the importance of appropriate transverse scaling and the use of elliptical scans for the assessment

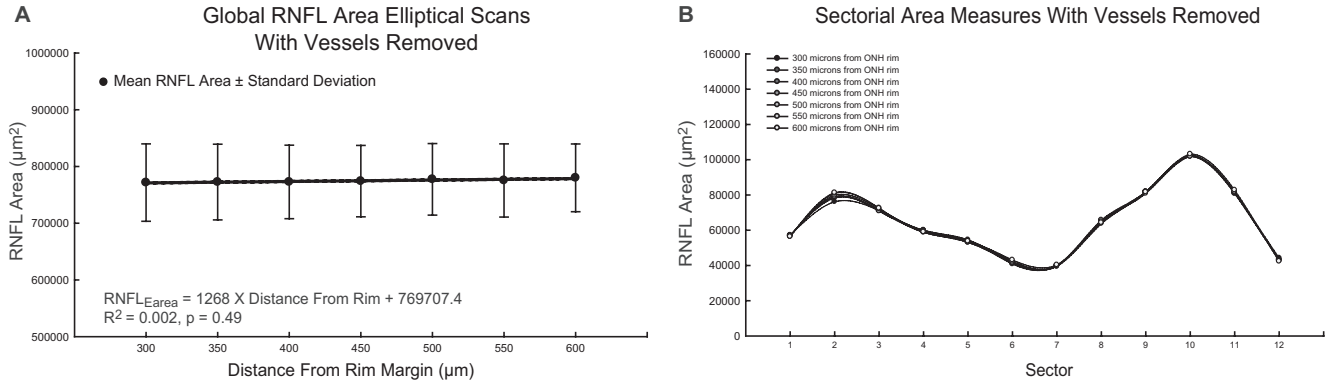

FIGURE 10. Area measures for global (**A**) and sectorial (**B**) RNFL showed no significant difference with increasing eccentricity from the ONH rim.

TABLE 6. Less Variability in RNFL Measures Are Noted after Appropriate Transverse Scaling Is Computed for Each Eye

	Without Vessel Compensation				With Vessel Compensation			
Scan Path	Global Thickness (μm)	COV (%)	Global Area (μm^2)	COV (%)	Global Thickness (μm)	COV (%)	Global Area (μm^2)	COV (%)
300	148.7	8.1	848628	8.4	135.1	8.2	771566	8.8
350	140.9	7.6	849681	8.1	128.2	7.9	772506	8.6
400	134.3	7.4	851540	7.8	121.9	8.0	772659	8.4
450	128.1	7.2	852310	7.8	116.4	7.4	774132	8.1
500	123.0	6.6	857253	7.5	111.5	7.2	777299	8.1
550	117.7	6.9	856979	7.6	106.5	7.5	775311	8.3
600	113.3	6.4	860773	7.3	102.6	6.8	779986	7.6
12°	115.2	11.0	846114	7.5	105.3	11.0	773221	7.9

Data for elliptical scans 300 to 600 μm from the rim margin and the standard 12° circular scan.

of the retinal nerve fiber layer. As an example, the data showed a significant relationship between axial length and RNFL thickness using the standard 12° circular scans. Although this result is in agreement with several studies in both human and nonhuman primates,[22–24,42,63] it is unlikely that it represents neuronal differences between longer and shorter eyes. In fact, the effect of ocular biometry was well explained by the differences in ocular magnification between subjects (Figs. 6A, 7), when axial length was eliminated as a factor by scaling the circular scan and expressing the results as RNFL areas. In essence, the relation between RNFL thickness and axial length occurs because a fixed angular scan covers a larger retinal region in longer compared with shorter eyes and RNFL tissue farther from the ONH margin is thinner.[25–27,31] The thinning associated with scan distance, however, does not reflect on a change in axonal content, but, rather, it is the change in axonal density with proximity to the optic nerve.[31,62]

The influence of ocular magnification is exemplified in the rhesus monkey, whose smaller eyes have higher equivalent powers. Overall, the slope of the relationship between RNFL thickness and axial length of the grouped data (−6.3 μm/mm) is significantly different from the (−2 to −3 μm/mm) regression slopes noted in human eyes.[22,24,28,64] Although, the major factor in ocular magnification is axial length, the longitudinal data from the seven animals illustrate the need to consider corneal curvature, anterior chamber depth, and ocular lens parameters. In these seven infants, even though area measures were similar between animals, the RNFL thickness relationship with axial length was significantly different between animals (Table 2). These differences in slope data could be explained by the different maturational rates of the ocular components in these animals.

Changes in RNFL thickness with increasing distance from the center of the optic nerve have been reported in a study in which SD-OCT technology was used in the nonhuman primate.[42] Similarly, the present findings indicate a linear change in thickness up to 600 μm from the rim margin. In addition, eyes with a larger global RNFL area have a greater change in RNFL thickness at increasing eccentricity (R^2 = 0.16, P = 0.01), with similar trends in each sector. However, this relationship becomes nonlinear when larger eccentricities are analyzed, as illustrated in RNFL thickness data up to 1050 μm from the rim margin in four animals (Fig. 12). It is important to note that the standard 12° circular scan path is within the region where changes in RNFL thickness follow this linear relationship.

Furthermore, systematic differences in scan paths and ocular magnification of various OCT systems may explain the differences in RNFL measures, using essentially similar technologies.[59,65,66] For example, Kang et al.[24] illustrated a method of minimizing the relationship of RNFL thickness and axial length, by accounting for ocular magnification based on the optical properties of the Cirrus HD OCT. In addition, using circular scans of various sizes, Bayraktar et al.[25] have shown significant changes in RNFL thickness, but minimal changes in RNFL area with increase in OCT scan diameter. Similarly, in nonhuman primates, RNFL area measures for elliptical scans 300 to 600 μm from the rim margin show no significant change. This finding is logical, as a reduction in axonal content is not expected in the regions analyzed. In accordance, we may find fewer discrepancies between various OCT technologies by accounting for ocular magnification.

For OCT measurements of the RNFL to be a good surrogate for the population of RGC axons, the contribution of non-

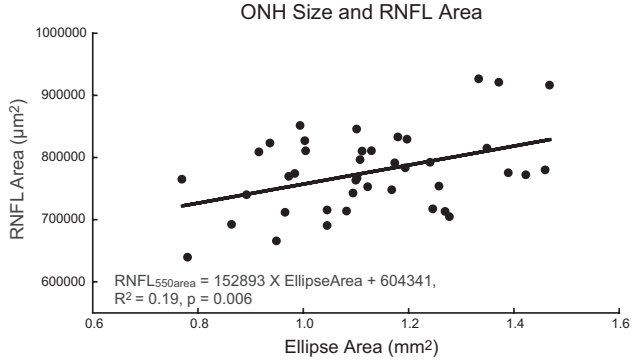

FIGURE 11. The relationship of RNFL thickness and RNFL area with size of the optic nerve.

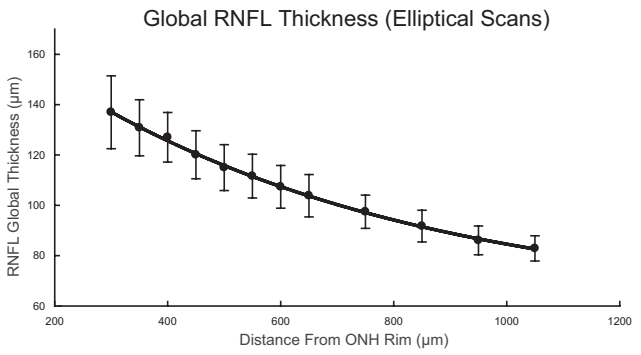

FIGURE 12. Change in global RNFL thickness in custom elliptical scans with increasing eccentricity from the rim margin.

neuronal components to the RNFL thickness or area should be considered.[67,68] The two main non-neuronal components within the nerve fiber layer include retinal blood vessels and neuroglia. With current OCT technologies, we are unable to account for glial components of the RNFL. However, retinal vessels within the retina are often seen as circular or elliptical structures that cast shadows on the underlying retina, and several retinal vessels usually pass through the nerve fiber layer in the region of the retina analyzed for RNFL thickness. After rescaling of OCT B-scans, many of these vessels take on a circular appearance, and this circular region can be subtracted from the total area. In the present study, retinal vasculature accounted for 9.3% of the total RNFL area in healthy nonhuman primate eyes. In human subjects, Hood et al.[53] predicted a ~13% contribution of retinal vasculature to the total RNFL thickness. The differences between the two studies could be due to methodology or the species being studied. Nonetheless, retinal vascular components make up a significant portion of the nerve fiber layer and, in glaucomatous eyes, the contribution may be larger, even though retinal vessels are thought to decrease by up to 15% in diameter.[53,69,70] For example, in animals with optic nerve transection, as the RNFL thickness deceases, retinal blood vessels are seen to emerge in the thickness plots as spikes.[71] These spikes in the TSNIT plot can be removed using methodology presented in this article, providing a better measure for the neuronal content of the RNFL. However, it is important to note that although the major retinal vessels are accounted for by the methods described, smaller vessels, which make a significant contribution to RNFL measures, cannot be accounted for by the current technology.[72,73]

RNFL area measurements should be linearly related to the number of RGC axons if, in addition to the vasculature, the non-neuronal glial components can be excluded from the area calculation (Wheat J, et al. *IOVS* 2007;48:ARVO E-Abstract 491; Wheat JL, et al. *IOVS* 2009;50:ARVO E-Abstract 5826). Such measures could reduce the variability noted in structure–function relationships. A previous nonhuman primate study indicated that the glial content in the nerve fiber layer is no less than 18%.[74] Although significant variations in glial content and activation are known to occur, especially with optic nerve and retinal disease processes, an estimate of 20% to 30% is reasonable to use for estimating axonal content in young, healthy eyes.[75–77] Several studies have also investigated axonal diameters of retinal ganglion cells. At the optic nerve, the mean axon diameter measures 0.84 ± 0.07 μm, with a cross-sectional area of 0.55 μm^2.[52,78] A reasonable estimate of the total axonal content in these healthy eyes can then be determined as:

$$\text{Estimated total number of axons in the RNFL} = \frac{\text{RNFL area with vessels removed} \times (1 - \text{estimated fraction of glial tissue in the RNFL})}{\text{Cross-sectional area of a single axon fiber}}.$$

In the RNFL cross-sectional areas, the axonal content of healthy rhesus primates is estimated at $1{,}126{,}953 \pm 92{,}198$ axons, using a 20% glial estimate, and is similar to that previously reported.[45,52,78,79]

Transverse scaling provides accurate data for the determination of the ONH shape and size. The size of the optic nerve for macaque monkeys (1.44 ± 0.19 μm^2) was similar to reported data using histologic methods.[39,44,45] Although a relationship between disc size and axial length have been reported in humans, this relationship was not seen in rhesus monkeys ($P = 0.14$).[80–83] However, the relationship between the size of the ONH and the RNFL area was significant and similar to relationships noted in previous human and nonhuman studies.[26,45]

In conclusion, the investigation of SD-OCT assessment of the RNFL suggests that scaled measures of the RNFL area can improve the interpretation of the retinal ganglion cell axonal content in the retina. After rescaling, RNFL thickness plots within the peripapillary region for scans of fixed distance from the rim margin can be constructed based on area measures. Although obtaining RNFL area measures requires the inclusion of ocular biometry data, there are fast, noninvasive methods available for these measurements.[84–86] The results also demonstrate the importance of using custom scans, especially in nonhuman primates, the majority of whom have an elliptical optic nerve.[22,26] Finally, while the use of an animal model with smaller eyes provides evidence that the methods of transverse scaling will be robust to normal ocular variations, the methods should be applied to normal human subjects and glaucoma patients to determine whether there is clinical utility for the diagnosis and management of glaucomatous neuropathy.

References

1. Quigley HA. Open-angle glaucoma. *N Engl J Med.* 1993;328:1097–1106.
2. Resnikoff S, Pascolini D, Etya'ale D, et al. Global data on visual impairment in the year 2002. *Bull World Health Organ.* 2004;82:844–851.
3. Sommer A, Miller NR, Pollack I, Maumenee AE, George T. The nerve fiber layer in the diagnosis of glaucoma. *Arch Ophthalmol.* 1977;95:2149–2156.
4. Quigley HA. Neuronal death in glaucoma. *Prog Retin Eye Res.* 1999;18:39–57.
5. Weinreb RN, Khaw PT. Primary open-angle glaucoma. *Lancet.* 2004;363:1711–1720.
6. Quigley HA, Miller NR, George T. Clinical evaluation of nerve fiber layer atrophy as an indicator of glaucomatous optic nerve damage. *Arch Ophthalmol.* 1980;98:1564–1571.
7. Harwerth RS, Vilupuru AS, Rangaswamy NV, Smith EL 3rd. The relationship between nerve fiber layer and perimetry measurements. *Invest Ophthalmol Vis Sci.* 2007;48:763–773.
8. Huang D, Swanson EA, Lin CP, et al. Optical coherence tomography. *Science.* 1991;254:1178–1181.
9. Sakamoto A, Hangai M, Yoshimura N. Spectral-domain optical coherence tomography with multiple B-scan averaging for enhanced imaging of retinal diseases. *Ophthalmology.* 2008;115:1071–1078 e1077.
10. Fujimoto JG. Optical coherence tomography for ultrahigh resolution in vivo imaging. *Nat Biotechnol.* 2003;21:1361–1367.
11. Wojtkowski M, Srinivasan V, Ko T, Fujimoto J, Kowalczyk A, Duker J. Ultrahigh-resolution, high-speed, Fourier domain optical coherence tomography and methods for dispersion compensation. *Opt Express.* 2004;12:2404–2422.
12. Sander B, Larsen M, Thrane L, Hougaard JL, Jorgensen TM. Enhanced optical coherence tomography imaging by multiple scan averaging. *Br J Ophthalmol.* 2005;89:207–212.

13. Carpineto P, Ciancaglini M, Zuppardi E, Falconio G, Doronzo E, Mastropasqua L. Reliability of nerve fiber layer thickness measurements using optical coherence tomography in normal and glaucomatous eyes. *Ophthalmology.* 2003;110:190–195.
14. Blumenthal EZ, Williams JM, Weinreb RN, Girkin CA, Berry CC, Zangwill LM. Reproducibility of nerve fiber layer thickness measurements by use of optical coherence tomography. *Ophthalmology.* 2000;107:2278–2282.
15. Schuman JS, Hee MR, Puliafito CA, et al. Quantification of nerve fiber layer thickness in normal and glaucomatous eyes using optical coherence tomography. *Arch Ophthalmol.* 1995;113:586–596.
16. Budenz DL, Fredette MJ, Feuer WJ, Anderson DR. Reproducibility of peripapillary retinal nerve fiber thickness measurements with stratus OCT in glaucomatous eyes. *Ophthalmology.* 2008;115: 661–666, e664.
17. Sung KR, Wollstein G, Schuman JS, et al. Scan quality effect on glaucoma discrimination by glaucoma imaging devices. *Br J Ophthalmol.* 2009;93:1580–1584.
18. Vizzeri G, Bowd C, Medeiros FA, Weinreb RN, Zangwill LM. Effect of improper scan alignment on retinal nerve fiber layer thickness measurements using Stratus optical coherence tomograph. *J Glaucoma.* 2008;17:341–349.
19. Vizzeri G, Bowd C, Medeiros FA, Weinreb RN, Zangwill LM. Effect of signal strength and improper alignment on the variability of stratus optical coherence tomography retinal nerve fiber layer thickness measurements. *Am J Ophthalmol.* 2009;148:249–255, e241.
20. Gabriele ML, Ishikawa H, Wollstein G, et al. Optical coherence tomography scan circle location and mean retinal nerve fiber layer measurement variability. *Invest Ophthalmol Vis Sci.* 2008;49: 2315–2321.
21. Kim JS, Ishikawa H, Sung KR, et al. Retinal nerve fibre layer thickness measurement reproducibility improved with spectral domain optical coherence tomography. *Br J Ophthalmol.* 2009; 93:1057–1063.
22. Budenz DL, Anderson DR, Varma R, et al. Determinants of normal retinal nerve fiber layer thickness measured by Stratus OCT. *Ophthalmology.* 2007;114:1046–1052.
23. Huynh SC, Wang XY, Rochtchina E, Mitchell P. Peripapillary retinal nerve fiber layer thickness in a population of 6-year-old children: findings by optical coherence tomography. *Ophthalmology.* 2006;113:1583–1592.
24. Kang SH, Hong SW, Im S, Lee S, Ahn MD. Effect of myopia on the thickness of the retinal nerve fiber layer measured by Cirrus HD optical coherence tomography. *Invest Ophthalmol Vis Sci.* 2010; 51:4075–4083.
25. Bayraktar S, Bayraktar Z, Yilmaz OF. Influence of scan radius correction for ocular magnification and relationship between scan radius with retinal nerve fiber layer thickness measured by optical coherence tomography. *J Glaucoma.* 2001;10:163–169.
26. Savini G, Zanini M, Carelli V, Sadun AA, Ross-Cisneros FN, Barboni P. Correlation between retinal nerve fibre layer thickness and optic nerve head size: an optical coherence tomography study. *Br J Ophthalmol.* 2005;89:489–492.
27. Skaf M, Bernardes AB, Cardillo JA, et al. Retinal nerve fibre layer thickness profile in normal eyes using third-generation optical coherence tomography. *Eye (Lond).* 2006;20:431–439.
28. Leung CK, Mohamed S, Leung KS, et al. Retinal nerve fiber layer measurements in myopia: An optical coherence tomography study. *Invest Ophthalmol Vis Sci.* 2006;47:5171–5176.
29. Bennett AG, Rudnicka AR, Edgar DF. Improvements on Littmann's method of determining the size of retinal features by fundus photography. *Graefes Arch Clin Exp Ophthalmol.* 1994;232:361–367.
30. Littmann H. Determination of the real size of an object on the fundus of the living eye (in German). *Klin Monbl Augenheilkd.* 1982;180:286–289.
31. Varma R, Skaf M, Barron E. Retinal nerve fiber layer thickness in normal human eyes. *Ophthalmology.* 1996;103:2114–2119.
32. Boothe RG, Kiorpes L, Williams RA, Teller DY. Operant measurements of contrast sensitivity in infant macaque monkeys during normal development. *Vision Res.* 1988;28:387–396.
33. Qiao-Grider Y, Hung LF, Kee CS, Ramamirtham R, Smith EL 3rd. Normal ocular development in young rhesus monkeys (Macaca mulatta). *Vision Res.* 2007;47:1424–1444.
34. Gaasterland D, Kupfer C. Experimental glaucoma in the rhesus monkey. *Invest Ophthalmol.* 1974;13:455–457.
35. Quigley HA, Hohman RM. Laser energy levels for trabecular meshwork damage in the primate eye. *Invest Ophthalmol Vis Sci.* 1983;24:1305–1307.
36. Harwerth RS, Smith EL 3rd, DeSantis L. Experimental glaucoma: perimetric field defects and intraocular pressure. *J Glaucoma.* 1997;6:390–401.
37. Harwerth RS. Primate glaucoma models. In: Pang IH, Clark AF, eds. *Animal Models for Retinal Disease*. New York: Humana Press; 2010:165–189.
38. Harwerth RS, Smith EL 3rd, DeSantis L. Behavioral perimetry in monkeys. *Invest Ophthalmol Vis Sci.* 1993;34:31–40.
39. Yang H, Downs JC, Sigal IA, Roberts MD, Thompson H, Burgoyne CF. Deformation of the normal monkey optic nerve head connective tissue after acute IOP elevation within 3-D histomorphometric reconstructions. *Invest Ophthalmol Vis Sci.* 2009;50:5785–5799.
40. Downs JC, Yang H, Girkin C, et al. Three-dimensional histomorphometry of the normal and early glaucomatous monkey optic nerve head: neural canal and subarachnoid space architecture. *Invest Ophthalmol Vis Sci.* 2007;48:3195–3208.
41. Sasaoka M, Nakamura K, Shimazawa M, Ito Y, Araie M, Hara H. Changes in visual fields and lateral geniculate nucleus in monkey laser-induced high intraocular pressure model. *Exp Eye Res.* 2008;86:770–782.
42. Fortune B, Yang H, Strouthidis NG, et al. The effect of acute intraocular pressure elevation on peripapillary retinal thickness, retinal nerve fiber layer thickness, and retardance. *Invest Ophthalmol Vis Sci.* 2009;50: 4719–4726.
43. Lapuerta P, Schein SJ. A four-surface schematic eye of macaque monkey obtained by an optical method. *Vision Res.* 1995;35: 2245–2254.
44. Strouthidis NG, Yang H, Fortune B, Downs JC, Burgoyne CF. Detection of optic nerve head neural canal opening within histomorphometric and spectral domain optical coherence tomography data sets. *Invest Ophthalmol Vis Sci.* 2009;50:214–223.
45. Quigley HA, Coleman AL, Dorman-Pease ME. Larger optic nerve heads have more nerve fibers in normal monkey eyes. *Arch Ophthalmol.* 1991;109:1441–1443.
46. Sanfilippo PG, Cardini A, Hewitt AW, Crowston JG, Mackey DA. Optic disc morphology: rethinking shape. *Prog Retin Eye Res.* 2009;28:227–248.
47. Mikelberg FS, Drance SM, Schulzer M, Yidegiligne HM, Weis MM. The normal human optic nerve: axon count and axon diameter distribution. *Ophthalmology.* 1989;96:1325–1328.
48. Mikelberg FS, Yidegiligne HM, White VA, Schulzer M. Relation between optic nerve axon number and axon diameter to scleral canal area. *Ophthalmology.* 1991;98:60–63.
49. Jonas JB, Schmidt AM, Muller-Bergh JA, Schlotzer-Schrehardt UM, Naumann GO. Human optic nerve fiber count and optic disc size. *Invest Ophthalmol Vis Sci.* 1992;33:2012–2018.
50. Panda-Jonas S, Jonas JB, Jakobczyk M, Schneider U. Retinal photoreceptor count, retinal surface area, and optic disc size in normal human eyes. *Ophthalmology.* 1994;101:519–523.
51. Ogden TE. Nerve fiber layer of the primate retina: morphometric analysis. *Invest Ophthalmol Vis Sci.* 1984;25:19–29.
52. Sanchez RM, Dunkelberger GR, Quigley HA. The number and diameter distribution of axons in the monkey optic nerve. *Invest Ophthalmol Vis Sci.* 1986;27:1342–1350.
53. Hood DC, Fortune B, Arthur SN, et al. Blood vessel contributions to retinal nerve fiber layer thickness profiles measured with optical coherence tomography. *J Glaucoma.* 2008;17:519–528.
54. Smith EL 3rd, Hung LF, Huang J. Relative peripheral hyperopic defocus alters central refractive development in infant monkeys. *Vision Res.* 2009;49:2386–2392.
55. Smith EL 3rd, Huang J, Hung LF, Blasdel TL, Humbird TL, Bockhorst KH. Hemiretinal form deprivation: evidence for local control of eye growth and refractive development in infant monkeys. *Invest Ophthalmol Vis Sci.* 2009;50:5057–5069.
56. Huang J, Hung LF, Ramamirtham R, et al. Effects of form deprivation on peripheral refractions and ocular shape in infant rhesus

monkeys (Macaca mulatta). *Invest Ophthalmol Vis Sci.* 2009;50: 4033–4044.
57. Bennett AG, Rabbetts RB. The schematic eye. In: Bennett AG, Rabbetts RB, eds. *Clinical Visual Optics*. London: Butterworths; 1989:249–274.
58. Kim JS, Ishikawa H, Gabriele ML, et al. Retinal nerve fiber layer thickness measurement comparability between time domain optical coherence tomography (OCT) and spectral domain OCT. *Invest Ophthalmol Vis Sci.* 2010;51:896–902.
59. Vizzeri G, Weinreb RN, Gonzalez-Garcia AO, et al. Agreement between spectral-domain and time-domain OCT for measuring RNFL thickness. *Br J Ophthalmol.* 2009;93:775–781.
60. Strouthidis NG, Yang H, Reynaud JF, et al. Comparison of clinical and spectral domain optical coherence tomography optic disc margin anatomy. *Invest Ophthalmol Vis Sci.* 2009;50:4709–4718.
61. Ramanujan S. Modular Equations and approximations to p. *Pure Appl Math Q.* 1913–1914;45:350–372.
62. Curcio CA, Allen KA. Topography of ganglion cells in human retina. *J Comp Neurol.* 1990;300:5–25.
63. Bendschneider D, Tornow RP, Horn FK, et al. Retinal nerve fiber layer thickness in normals measured by spectral domain OCT. *J Glaucoma.* 2009;19:475–482.
64. Hougaard JL, Ostenfeld C, Heijl A, Bengtsson B. Modelling the normal retinal nerve fibre layer thickness as measured by Stratus optical coherence tomography. *Graefes Arch Clin Exp Ophthalmol.* 2006;244:1607–1614.
65. Huang J, Liu X, Wu Z, et al. Macular and retinal nerve fiber layer thickness measurements in normal eyes with the Stratus OCT, the Cirrus HD-OCT, and the Topcon 3D OCT-1000. *J Glaucoma.* Published online April 29, 2010.
66. Savini G, Carbonelli M, Barboni P. Retinal nerve fiber layer thickness measurement by Fourier-domain optical coherence tomography: a comparison between cirrus-HD OCT and RTVue in healthy eyes. *J Glaucoma.* 2010;19:369–372.
67. Harwerth RS, Wheat JL, Rangaswamy NV. Age-related losses of retinal ganglion cells and axons. *Invest Ophthalmol Vis Sci.* 2008; 49:4437–4443.
68. Harwerth RS, Wheat JL, Fredette MJ, Anderson DR. Linking structure and function in glaucoma. *Prog Retin Eye Res.* 2010;29:249–271.
69. Jonas JB, Fernandez MC, Naumann GO. Parapapillary atrophy and retinal vessel diameter in nonglaucomatous optic nerve damage. *Invest Ophthalmol Vis Sci.* 1991;32:2942–2947.
70. Rader J, Feuer WJ, Anderson DR. Peripapillary vasoconstriction in the glaucomas and the anterior ischemic optic neuropathies. *Am J Ophthalmol.* 1994;117:72–80.
71. Fortune B, Cull GA, Burgoyne CF. Relative course of retinal nerve fiber layer birefringence and thickness and retinal function changes after optic nerve transection. *Invest Ophthalmol Vis Sci.* 2008;49:4444–4452.
72. Scoles D, Gray DC, Hunter JJ, et al. In-vivo imaging of retinal nerve fiber layer vasculature: imaging histology comparison. *BMC Ophthalmol.* 2009;9:9.
73. Ogden TE. Nerve fiber layer of the macaque retina: retinotopic organization. *Invest Ophthalmol Vis Sci.* 1983;24:85–98.
74. Ogden TE. Nerve fiber layer of the primate retina: thickness and glial content. *Vision Res.* 1983;23:581–587.
75. Lam TT, Kwong JM, Tso MO. Early glial responses after acute elevated intraocular pressure in rats. *Invest Ophthalmol Vis Sci.* 2003;44:638–645.
76. Nickells RW. From ocular hypertension to ganglion cell death: a theoretical sequence of events leading to glaucoma. *Can J Ophthalmol.* 2007;42:278–287.
77. Tezel G. The role of glia, mitochondria, and the immune system in glaucoma. *Invest Ophthalmol Vis Sci.* 2009;50:1001–1012.
78. Cull G, Cioffi GA, Dong J, Homer L, Wang L. Estimating normal optic nerve axon numbers in non-human primate eyes. *J Glaucoma.* 2003;12:301–306.
79. Morrison JC, Cork LC, Dunkelberger GR, Brown A, Quigley HA. Aging changes of the rhesus monkey optic nerve. *Invest Ophthalmol Vis Sci.* 1990;31:1623–1627.
80. Nangia V, Matin A, Bhojwani K, Kulkarni M, Yadav M, Jonas JB. Optic disc size in a population-based study in central India: the Central India Eye and Medical Study (CIEMS). *Acta Ophthalmol.* 2008;86:103–104.
81. Wang Y, Xu L, Zhang L, Yang H, Ma Y, Jonas JB. Optic disc size in a population based study in northern China: the Beijing Eye Study. *Br J Ophthalmol.* 2006;90:353–356.
82. Xu L, Li Y, Wang S, Wang Y, Jonas JB. Characteristics of highly myopic eyes: the Beijing Eye Study. *Ophthalmology.* 2007;114: 121–126.
83. Samarawickrama C, Wang XY, Huynh SC, Burlutsky G, Stapleton F, Mitchell P. Effects of refraction and axial length on childhood optic disk parameters measured by optical coherence tomography. *Am J Ophthalmol.* 2007;144:459–461.
84. Rajan MS, Keilhorn I, Bell JA. Partial coherence laser interferometry vs conventional ultrasound biometry in intraocular lens power calculations. *Eye* (*Lond*). 2002;16:552–556.
85. Liampa Z, Kynigopoulos M, Pallas G, Gerding H. Comparison of two partial coherence interferometry devices for ocular biometry. *Klin Monbl Augenheilkd.* 2010;227:285–288.
86. Holzer MP, Mamusa M, Auffarth GU. Accuracy of a new partial coherence interferometry analyser for biometric measurements. *Br J Ophthalmol.* 2009;93:807–810.